Article

Magnetospheric origin of a fast radio burst constrained using scintillation

https://doi.org/10.1038/s41586-024-08297-w

Received: 14 June 2024

Accepted: 28 October 2024

Published online: 1 January 2025

Check for updates

Kenzie Nimmo[1]✉, Ziggy Pleunis[2,3,4], Paz Beniamini[5,6], Pawan Kumar[7], Adam E. Lanman[1,8], D. Z. Li[9], Robert Main[10,11], Mawson W. Sammons[10,11], Shion Andrew[1,8], Mohit Bhardwaj[12], Shami Chatterjee[13], Alice P. Curtin[10,11], Emmanuel Fonseca[14,15], B. M. Gaensler[2,16,17], Ronniy C. Joseph[10,11], Zarif Kader[10,11], Victoria M. Kaspi[10,11], Mattias Lazda[2,16], Calvin Leung[18], Kiyoshi W. Masui[1,8], Ryan Mckinven[10,11], Daniele Michilli[1,8], Ayush Pandhi[2,16], Aaron B. Pearlman[10,11], Masoud Rafiei-Ravandi[10,11], Ketan R. Sand[10,11], Kaitlyn Shin[1,8], Kendrick Smith[19] & Ingrid H. Stairs[20]

Fast radio bursts (FRBs) are microsecond-to-millisecond-duration radio transients[1] that originate mostly from extragalactic distances. The FRB emission mechanism remains debated, with two main competing classes of models: physical processes that occur within close proximity to a central engine[2–4]; and relativistic shocks that propagate out to large radial distances[5–8]. The expected emission-region sizes are notably different between these two types of models[9]. Here we present the measurement of two mutually coherent scintillation scales in the frequency spectrum of FRB 20221022A[10]: one originating from a scattering screen located within the Milky Way, and the second originating from its host galaxy or local environment. We use the scattering media as an astrophysical lens to constrain the size of the observed FRB lateral emission region[9] to $\lesssim 3 \times 10^4$ kilometres. This emission size is inconsistent with the expectation for the large-radial-distance models[5–8], and is more naturally explained by an emission process that operates within or just beyond the magnetosphere of a central compact object. Recently, FRB 20221022A was found to exhibit an S-shaped polarization angle swing[10], most likely originating from a magnetospheric emission process. The scintillation results presented in this work independently support this conclusion, while highlighting scintillation as a useful tool in our understanding of FRB emission physics and progenitors.

Inhomogeneities in the interstellar medium cause the radio waves from point sources to scatter, which results in temporal broadening of the signal[11] (parameterized by the scattering timescale τ_s at some reference frequency). Scattering creates a stochastic interference pattern on the signal, called scintillation, corresponding to a frequency-dependent intensity modulation (parameterized by the characteristic frequency scale, known as the decorrelation bandwidth $\Delta\nu_{DC}$ specified at some frequency)[11]. Temporal broadening becomes larger towards lower frequencies, $\tau_s \propto \nu^{-\alpha}$, for observing frequency ν, and spectral 'scintles' become wider towards higher frequencies, $\Delta\nu_{DC} \propto \nu^{\alpha}$. The index α is often close to the expectation from Gaussian density fluctuations in the scattering medium, $\alpha = 4$. Moreover, scattering and scintillation are inversely proportional[12]: $\tau_s \approx C/(2\pi\Delta\nu_{DC})$, with C in the range of 1–2. Scattering and/or scintillation measurements in the radio signal are a powerful probe of interstellar optics[13]. Such measurements have been used to resolve emission regions in the Crab Pulsar[14]; measure relativistic motion in Crab Pulsar giant pulses[15]; constrain the size of a gamma-ray burst afterglow[16]; probe the circumburst environment of fast radio bursts (FRBs)[17]; and have the potential to probe the structure of the circumgalactic medium (for example, refs. 18,19).

The Canadian Hydrogen Intensity Mapping Experiment (CHIME) FRB project[20] recently discovered the as-yet non-repeating FRB 20221022A[10], with a signal-to-noise ratio (S/N) of 64.9. The event was processed using the CHIME/FRB baseband pipeline[21], which produced a beamformed data product containing complex voltages for both the X and the Y polarization hands, with a time and frequency resolution of 2.56 μs

[1]MIT Kavli Institute for Astrophysics and Space Research, Massachusetts Institute of Technology, Cambridge, MA, USA. [2]Dunlap Institute for Astronomy and Astrophysics, University of Toronto, Toronto, Ontario, Canada. [3]Anton Pannekoek Institute for Astronomy, University of Amsterdam, Amsterdam, The Netherlands. [4]ASTRON, Netherlands Institute for Radio Astronomy, Dwingeloo, The Netherlands. [5]Department of Natural Sciences, The Open University of Israel, Ra'anana, Israel. [6]Astrophysics Research Center of the Open university (ARCO), The Open University of Israel, Ra'anana, Israel. [7]Department of Astronomy, University of Texas at Austin, Austin, TX, USA. [8]Department of Physics, Massachusetts Institute of Technology, Cambridge, MA, USA. [9]Department of Astrophysical Sciences, Princeton University, Princeton, NJ, USA. [10]Trottier Space Institute, McGill University, Montreal, Quebec, Canada. [11]Department of Physics, McGill University, Montreal, Quebec, Canada. [12]McWilliams Center for Cosmology, Department of Physics, Carnegie Mellon University, Pittsburgh, PA, USA. [13]Cornell Center for Astrophysics and Planetary Science, Cornell University, Ithaca, NY, USA. [14]Department of Physics and Astronomy, West Virginia University, Morgantown, WV, USA. [15]Center for Gravitational Waves and Cosmology, West Virginia University, Morgantown, WV, USA. [16]Department of Astronomy and Astrophysics, University of California Santa Cruz, Santa Cruz, CA, USA. [17]David A. Dunlap Department of Astronomy and Astrophysics, University of Toronto, Toronto, Ontario, Canada. [18]Department of Astronomy, University of California Berkeley, Berkeley, CA, USA. [19]Perimeter Institute for Theoretical Physics, Waterloo, Ontario, Canada. [20]Department of Physics and Astronomy, University of British Columbia, Vancouver, British Columbia, Canada. ✉e-mail: knimmo@mit.edu

and 0.39 MHz, respectively. The FRB was localized[10,21] to equatorial coordinates right ascension (J2000) = 03 h 14 min 31 s(22), declination (J2000) = +86° 52′ 19″(14) (where the uncertainties quoted are 1σ confidence levels), and associated with a host galaxy at a redshift of 0.0149(3) with posterior probability ≳99%.

The beamformed baseband data were coherently and incoherently dedispersed to a dispersion measure of 116.837 pc cm^{-3}, measured by maximizing the structure in the burst[10,22]. The data were then upchannelized to a frequency resolution of 0.76 kHz (Methods), at the expense of time resolution. This frequency resolution is the highest we can achieve before diluting the signal with noise, given the total width of the FRB (about 2 ms; Extended Data Fig. 1). This resolution is sufficiently high to allow us to probe the expected decorrelation bandwidth from the Milky Way interstellar medium (52 kHz at 600 MHz: estimated from the NE2001 Galactic electron density model[23,24]). The autocorrelation function (ACF; Methods) of the upchannelized spectrum (that is, the flux density as a function of frequency integrated over the 2-ms burst duration), was then computed and is shown in Fig. 1. For a burst spectrum that shows intensity fluctuations owing to scintillation, the expected functional form of the ACF is a Lorentzian where the half-width at half-maximum is the decorrelation bandwidth[25]. In addition, the ACF that we compute is normalized such that the peak of the Lorentzian is the square of the modulation index (Methods), defined as the standard deviation of the observed spectrum divided by its mean[25]. Three distinct frequency scales are evident in the ACF (Fig. 1). The approximately 30-MHz scale, which is also apparent in the burst dynamic spectrum (Extended Data Fig. 1), is not scintillation, but rather introduced by reflections between the mesh and the focal line (separated by 5 m) of the semi-cylindrical CHIME reflectors[26]. We confirm that the other 2 frequency scales are both scintillation from 2 distinct scattering screens by computing the ACF for 8 subbands across the CHIME observing band of 400–800 MHz, containing an equal fraction of the burst energy, measuring both scales in each subband, and observing that they evolve with frequency with index $\alpha = 3.7 \pm 0.6$ and $\alpha = 3.2 \pm 0.3$ for the frequency scales $\Delta\nu_{DC} = 6 \pm 1$ kHz and $\Delta\nu_{DC} = 128 \pm 6$ kHz at 600 MHz, respectively (Fig. 2 and Methods). Scaling our scintillation measurements to 1 GHz using the measured α, we are able to compare with the Milky Way scattering prediction (τ_s at 1 GHz)[23]. We find that the 6-kHz scintillation scale is a factor of about 10 less than the prediction, whereas the 128-kHz scale is a factor of about 1.6 larger. Naively, one might expect 128 kHz to be the Galactic scintillation scale owing to its better agreement with predictions; however, it is worth noting that Galactic electron density models have large uncertainties (for example, as discussed in ref. 27), especially for lines of sight at high Galactic latitude, b, as is the case for FRB 20221022A ($b \approx 24.6°$).

Measuring two scintillation scales implies that those screens are sufficiently distant from each other that the screen closest to the observer is not resolving out the farther screen. We use this to show that if both screens were in the Milky Way, coherence would not be maintained and we would not have measured a second scintillation scale (Methods). We know that FRB 20221022A is extragalactic because of its host-galaxy association[10] with posterior probability ≳99%, confirming that screen s_2 is also extragalactic. Moreover, we place the following constraint on the product of the distance between the FRB and the extragalactic screen, $d_{s_2\star}$, and the observer to Galactic screen distance $d_{\oplus s_1}$: $d_{\oplus s_1} d_{s_2\star} \lesssim 9.1$ kpc^2 (Methods).

To identify which scintillation scale originates from the extragalactic screen, we consider the modulation indices: $m_{6kHz} = 1.2 \pm 0.1$ and $m_{128kHz} = 0.78 \pm 0.08$, for the 6-kHz and 128-kHz scintillation scales, respectively (Methods). Over the observing band, the modulation index of both scintillation scales are consistent with being constant (Fig. 2). m_{6kHz} is consistent with order unity, which indicates 'perfect' modulation from a point source. We observe that $m_{128kHz} < m_{6kHz}$. For the screen closest to the observer, a modulation index <1 would imply that the screen is partially resolving the farther screen. For the screen closest to the FRB, a modulation index <1 would imply that the screen is partially resolving the FRB emission region. We find no strong frequency dependence of the 128-kHz scale modulation index, and we measure a decorrelation-bandwidth frequency evolution closer to ν^3 than ν^4 (Fig. 2), both of which are more in support of the latter scenario (Methods). We therefore place the 128-kHz screen closest to the FRB and the 6-kHz screen closest to the observer. In Methods, we also consider the case where the order of the screens is flipped, and show that

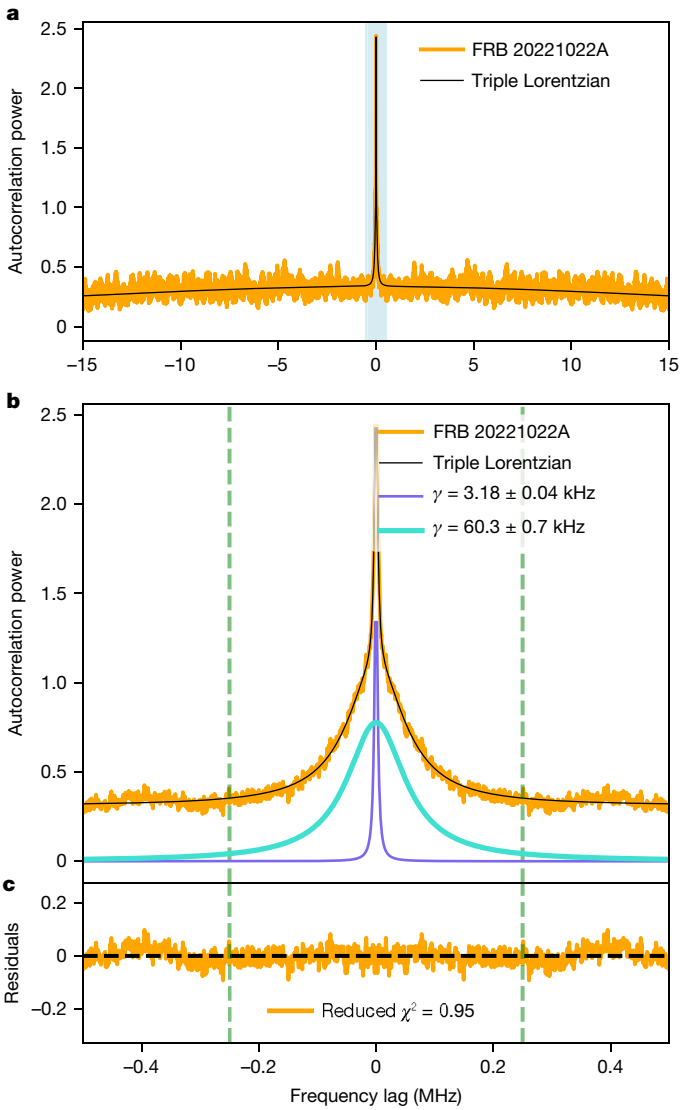

Fig. 1 | Three frequency scales evident in the full-band ACF of the FRB 20221022A spectrum. a, The ACF, with a frequency resolution of 0.76 kHz, in the lag range −15 MHz to +15 MHz. **b**, Zoom-in on the central lag range of the ACF, highlighted by the shaded blue region in **a**. The black line represents a triple Lorentzian (equation (2)) fit to the ACF between ±20 MHz (**a**) and ±0.5 MHz (**b**). The larger frequency scale, most clearly observable in **a** (half-width at half-maximum $\gamma = 27.3 \pm 0.1$ MHz), is attributed to an instrumental ripple existing in CHIME/FRB data. The two smaller scales, which are more clearly observed in **b**, are attributed to scintillation with decorrelation bandwidths of 3.18 ± 0.04 kHz and 60.3 ± 0.7 kHz: the individual Lorentzians are plotted in **b** in purple and blue, respectively. **c**, The residuals. The reduced χ^2 is computed within the lag range ±0.25 MHz, highlighted by the green dashed lines. We reduce the lag range as the approximately 30-MHz frequency scale is not expected to show a Lorentzian functional form. The scintillation scales, however, are expected to be Lorentzian in form, and we find a reduced χ^2 very close to 1, implying a good fit to the data.

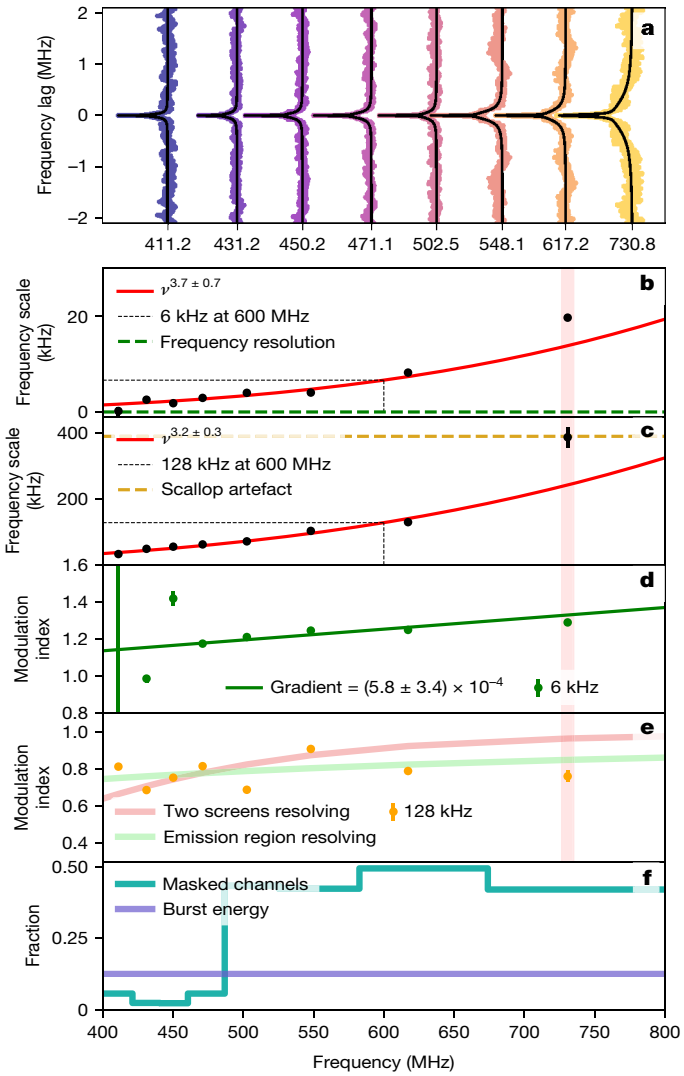

Fig. 2 | Confirming two scintillation scales in the FRB 20221022A spectrum, with decorrelation bandwidths 6 ± 1 kHz and 128 ± 6 kHz at 600 MHz. **a**, The ACFs calculated for 8 subbands containing an equal fraction of the burst energy at a frequency resolution of 0.76 kHz. Overplotted in black is a double Lorentzian fit to each ACF. **b**,**c**, Two frequency scales are measured in each subband (smaller scale in **b**, and larger in **c**), and are fit with the functional form $A\nu^{\alpha}$, for constant A and index α, shown in red. The horizontal dashed green line in **b** is the resolution and the yellow dashed horizontal line in **c** is the upchannelization artefact. In **b** and **c**, the measured decorrelation bandwidths at 600 MHz are marked with black dashed lines. **d**,**e**, The modulation indices for the 6-kHz (**d**) and 128-kHz (**e**) frequency scales across the band. A least-squares fit of a straight line is overplotted on **d** (dark green) and we fit the expected evolution of the modulation index with frequency for a screen resolving the emission-region size (light green; equation (22)) as well as the expected evolution for the screens resolving each other (pink; equation (23)) to the 128-kHz modulation indices in **e**. Error bars (1σ) are plotted for all frequency scales and modulation indices, noting that they are often too small to distinguish from the marker. In **b**–**e**, the high-frequency data point has been omitted from all fits, indicated by the shaded red region, owing to the ambiguity of the scintillation scale and the upchannelization artefacts. Omitting the lowest-frequency measurement for the 6-kHz scale, where the modulation index uncertainties are large, does not affect the measurements. **f**, The number of masked channels per subband (turquoise), and the fraction of the burst energy per subband (purple).

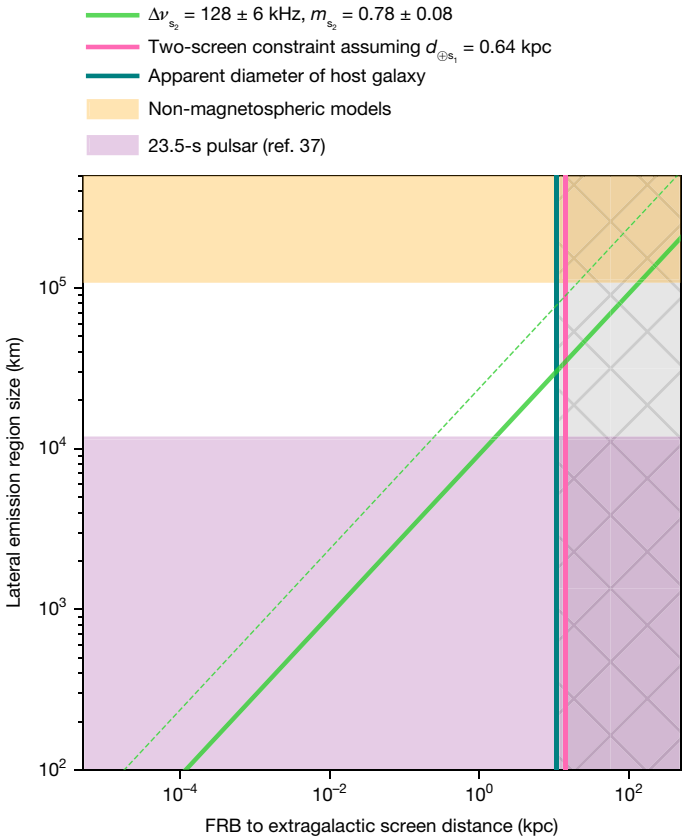

Fig. 3 | The degeneracy between the lateral emission-region size and the FRB to extragalactic screen distance. For the scintillation measurements $\Delta\nu_{s_2}$ = 128 ± 6 kHz and m_{s_2} = 0.78 ± 0.08, the green line represents the allowable combinations of emission size and source–screen separations (with the 3σ uncertainty upper bound indicated by the dashed green line, calculated by propagating the $\Delta\nu_{s_2}$ and m_{s_2} errors using equation (22)). The vertical pink line indicates the two-screen constraint on the source–screen distance, $d_{s_2\star} \lesssim 14.1$ kpc, assuming a Galactic screen distance of 0.64 kpc from NE2001[23]. This Galactic screen distance assumption is highly uncertain, and we explore its effect on the emission size in Extended Data Fig. 5. The vertical dark teal line indicates the apparent diameter of the FRB host galaxy measured in the optical (11 kpc)[30]. The grey hatched region shows the extragalactic screen distances we rule out. The orange shaded region indicates the observed emission sizes, $R_{\star\mathrm{obs}}$, inferred from the radial distances, d, for far-away shock models[5–8]. The purple shaded region indicates the possible emission sizes for the slowest known pulsar[37] (which therefore has the largest magnetosphere of known radio pulsars).

it only strengthens the constraint on the FRB emission-region size. Consequently, the FRB emission region is being partially resolved by the 128-kHz scintillation screen. This means that the angular size of the emission region projected onto the extragalactic screen is slightly larger than the diffractive scale of the screen[9]. Naturally, this introduces a degeneracy between the emission size and screen–source distance: a larger physical emission size with a screen in the outskirts of the galaxy or a small physical emission size with a very nearby screen could result in the same projected angular size. We plot the allowable screen–source distance and lateral emission-region size combinations in Fig. 3.

FRB emission models are broadly grouped into two categories: one where the emission originates from within the magnetosphere of a compact object[2–4], and a second where relativistic shocks propagate far from a central engine and produce coherent radio emission at large radial distances[5–8]. In the latter class of models, irrespective of the exact FRB emission mechanism (for example, synchrotron maser[28]), one can relate the lateral emission-region size, $R_{\star\mathrm{obs}}$, to the FRB emission site distance, d, from the central compact object[9]: $d \approx R_{\star\mathrm{obs}}\gamma \approx \frac{R^2_{\star\mathrm{obs}}}{2c\Delta t}$, where Δt is the FRB temporal duration and γ is the Lorentz factor of the shock. For the far-away models[5–8], radial distances range from 10^7 km to 10^{11} km, which corresponds to $R_{\star\mathrm{obs}} \approx 10^5$–$10^7$ km given our observed FRB duration: $\Delta t \approx 2$ ms (Extended Data Fig. 1). We require an FRB to screen

distance of $d_{s_2\star} \gtrsim 144$ kpc to have emission sizes consistent with the non-magnetospheric models (Fig. 3). It is unlikely that the screen is at such large distances, far out in the circumgalactic medium of the host galaxy. This is because (1) the implied densities ($n_e \approx O(10^{-3}\,\mathrm{cm}^{-3})$, calculated using equations (4) and (5) from ref. 9) are at least an order of magnitude higher than the current best estimate for the Milky Way circumgalactic medium at the same distance[29]; (2) from the two-screen constraints mentioned earlier, the Galactic screen distance would have to be $\lesssim$63 pc to satisfy the inequality (Extended Data Fig. 5); and (3) the FRB source would need to be outside of the host-galaxy disk to explain why we do not measure scattering or scintillation from the disk (where the densities are higher). Following these arguments, we find that it is most plausible that the extragalactic screen is constrained to be within the host-galaxy disk, allowing us to place the conservative constraint on $d_{s_2\star}$ from the apparent diameter of the host galaxy as observed in optical light (11 kpc)[30]. It is worth noting that the electron distribution extends farther than the optical diameter of the galaxy; however, the inclination of the galaxy as well as the low inferred host dispersion measure[10] imply that the FRB is not traversing through the full length of the galaxy and therefore 11 kpc is a highly conservative upper limit on the screen distance. With this upper limit on $d_{s_2\star}$, we constrain the observed emission size of $R_{\star\mathrm{obs}} \lesssim 3 \times 10^4$ km (Fig. 3).

The FRB emission size constraints presented here support an emission process that occurs within, or just beyond[15,31], the magnetosphere of a compact object. Our findings independently support the conclusions drawn on FRB 20221022A in ref. 10. There the authors observed an S-shaped polarization position angle swing across the burst duration, often seen in pulsar pulses and attributed to an emission beam sweeping across the line of sight, indicative of a magnetospheric origin of the emission. The discovery of subsecond periodicity in an FRB[32], (sub) microsecond timescales in some repeating FRBs[33,34], and magnetar spin-down glitches coinciding with FRB-like emission[35] support the magnetospheric class of FRB emission models. However, the diversity of spectro-temporal properties observed, even for a single repeating source[36], sparks debates about whether multiple emission mechanisms are at play. This work highlights incredible potential for similar scintillation studies in the future to explore both the emission physics of FRBs and the properties of their immediate environments, which hold valuable clues to their sources and progenitors.

Online content

Any methods, additional references, Nature Portfolio reporting summaries, source data, extended data, supplementary information, acknowledgements, peer review information; details of author contributions and competing interests; and statements of data and code availability are available at https://doi.org/10.1038/s41586-024-08297-w.

1. Petroff, E., Hessels, J. W. T. & Lorimer, D. R. Fast radio bursts at the dawn of the 2020s. *Astron. Astrophys. Rev.* **30**, 2 (2022).
2. Kumar, P., Lu, W. & Bhattacharya, M. Fast radio burst source properties and curvature radiation model. *Mon. Not. R. Astron. Soc.* **468**, 2726–2739 (2017).
3. Lyutikov, M. & Popov, S. Fast radio bursts from reconnection events in magnetar magnetospheres. Preprint at https://arxiv.org/abs/2005.05093 (2020).
4. Lyutikov, M. Coherent emission in pulsars, magnetars, and fast radio bursts: reconnection-driven free electron laser. *Astrophys. J.* **922**, 166 (2021).
5. Lyubarsky, Y. A model for fast extragalactic radio bursts. *Mon. Not. R. Astron. Soc.* **442**, L9–L13 (2014).
6. Metzger, B. D., Margalit, B. & Sironi, L. Fast radio bursts as synchrotron maser emission from decelerating relativistic blast waves. *Mon. Not. R. Astron. Soc.* **485**, 4091–4106 (2019).
7. Margalit, B., Metzger, B. D. & Sironi, L. Constraints on the engines of fast radio bursts. *Mon. Not. R. Astron. Soc.* **494**, 4627–4644 (2020).
8. Beloborodov, A. M. Blast waves from magnetar flares and fast radio bursts. *Astrophys. J.* **896**, 142 (2020).
9. Kumar, P., Beniamini, P., Gupta, O. & Cordes, J. M. Constraining the FRB mechanism from scintillation in the host galaxy. *Mon. Not. R. Astron. Soc.* **527**, 457–470 (2024).
10. Mckinven, R. et al. A pulsar-like swing polarization angle swing from a nearby nearby fast radio burst. *Nature* https://doi.org/10.1038/s41586-024-08184-4 (2024).
11. Rickett, B. J. Interstellar scattering and scintillation of radio waves. *Ann. Rev. Astron. Astrophys.* **15**, 479–504 (1977).
12. Cordes, J. M. & Rickett, B. J. Diffractive interstellar scintillation timescales and velocities. *Astrophys. J.* **507**, 846–860 (1998).
13. Gwinn, C. R. et al. Interstellar optics. *Astrophys. J.* **505**, 928–940 (1998).
14. Main, R. et al. Resolving the emission regions of the Crab Pulsar's giant pulses. *Astrophys. J.* **915**, 65 (2021).
15. Lin, R. et al. Resolving the emission regions of the Crab Pulsar's giant pulses. II. Evidence for relativistic motion. *Astrophys. J.* **945**, 115 (2023).
16. Frail, D. A., Kulkarni, S. R., Nicastro, L., Feroci, M. & Taylor, G. B. The radio afterglow from the γ-ray burst of 8 May 1997. *Nature* **389**, 261–263 (1997).
17. Masui, K. et al. Dense magnetized plasma associated with a fast radio burst. *Nature* **528**, 523–525 (2015).
18. Vedantham, H. K. & Phinney, E. S. Radio wave scattering by circumgalactic cool gas clumps. *Mon. Not. R. Astron. Soc.* **483**, 971–984 (2019).
19. Jow, D. L., Wu, X. & Pen, U.-L. Refractive lensing of scintillating FRBs by sub-parsec cloudlets in the multi-phase CGM. *Proc. Natl Acad. Sci. USA* **121**, e2406783121 (2024).
20. CHIME/FRB Collaboration et al. The CHIME fast radio burst project: system overview. *Astrophys. J.* **863**, 48 (2018).
21. Michilli, D. et al. An analysis pipeline for CHIME/FRB full-array baseband data. *Astrophys. J.* **910**, 147 (2021).
22. Seymour, A., Michilli, D. & Pleunis, Z. DM_phase: algorithm for correcting dispersion of radio signals. *Astrophysics Source Code Library* ascl:1910.004 (2019).
23. Cordes, J. M. & Lazio, T. J. W. NE2001. I. A new model for the galactic distribution of free electrons and its fluctuations. Preprint at https://arxiv.org/abs/astro-ph/0207156 (2002).
24. Ocker, S. K. & Cordes, J. M. NE2001p: a native Python implementation of the NE2001 galactic electron density model. *Res. Not. Am. Astron. Soc.* **8**, 17 (2024).
25. Rickett, B. J. Radio propagation through the turbulent interstellar plasma. *Ann. Rev. Astron. Astrophys.* **28**, 561–605 (1990).
26. CHIME Collaboration et al. An overview of CHIME, the Canadian Hydrogen Intensity Mapping Experiment. *Astrophys. J. Suppl. Ser.* **261**, 29 (2022).
27. Gaensler, B. M., Madsen, G. J., Chatterjee, S. & Mao, S. A. The vertical structure of warm ionised gas in the Milky Way. *Pub. Astron. Soc. Aust.* **25**, 184–200 (2008).
28. Macquart, J. P. et al. The spectral properties of the bright fast radio burst population. *Astrophys. J. Lett.* **872**, L19 (2019).
29. Voit, G. M. Ambient column densities of highly ionized oxygen in precipitation-limited circumgalactic media. *Astrophys. J.* **880**, 139 (2019).
30. Paturel, G. et al. HYPERLEDA. I. Identification and designation of galaxies. *Astron. Astrophys.* **412**, 45–55 (2003).
31. Philippov, A., Uzdensky, D. A., Spitkovsky, A. & Cerutti, B. Pulsar radio emission mechanism: radio nanoshots as a low-frequency afterglow of relativistic magnetic reconnection. *Astrophys. J. Lett* **876**, L6 (2019).
32. Chime/FRB Collaboration et al. Sub-second periodicity in a fast radio burst. *Nature* **607**, 256–259 (2022).
33. Nimmo, K. et al. Highly polarized microstructure from the repeating FRB 20180916B. *Nat. Astron.* **5**, 594–603 (2021).
34. Nimmo, K. et al. Burst timescales and luminosities as links between young pulsars and fast radio bursts. *Nat. Astron.* **6**, 393–401 (2022).
35. Younes, G. et al. Magnetar spin-down glitch clearing the way for FRB-like bursts and a pulsed radio episode. *Nat. Astron.* **7**, 339–350 (2023).
36. Hewitt, D. M. et al. Dense forests of microshots in bursts from FRB 20220912A. *Mon. Not. R. Astron. Soc.* **526**, 2039–2057 (2023).
37. Tan, C. M. et al. LOFAR discovery of a 23.5 s radio pulsar. *Astrophys. J.* **866**, 54 (2018).

Methods

Scintillation analysis

To measure scintillation, the coherently dedispersed baseband data were first upchannelized to a frequency resolution of 0.76 kHz. The upchannelization process was as follows: first the complex voltage dynamic spectrum was divided into time blocks of length 512 bins; for each polarization hand, frequency channel and time block, a fast Fourier transform was performed, creating an array that has a single polarization hand, a single time bin and 512 frequency channels; the result was a complex voltage dynamic spectrum with 2 polarization hands, 2.56 × 512 μs time resolution, and 0.390625/512-MHz frequency resolution, where 0.390625 MHz is the original channelization of the baseband data: 400 MHz over 1,024 channels. This frequency resolution was chosen to probe the expected decorrelation bandwidth from the Milky Way interstellar medium, estimated using NE2001 (44 kHz at 600 MHz; using $\tau_{s,1GHz} \approx 0.46$ μs from refs. 23,24 and the relationship $\tau_s \approx 1/(2\pi\Delta\nu_{DC})$).

In the upchannelized data product, the time resolution is sufficiently coarse such that the burst is unresolved in time. The on-burst spectrum is then taken to be the maximum S/N time bin. An off-burst spectrum is also computed for calibration purposes. The fast Fourier transform used to upchannelize the baseband data introduces a scalloping artefact that repeats every 0.390625 MHz (that is, the width of the channels of the original channelization of the baseband data). To correct for this artefact, the off-burst spectrum was folded to determine an average 0.390625-MHz scallop shape, which was then divided out from the on-burst spectrum (Extended Data Fig. 2). We attributed channels in the off-burst spectrum that exceed an S/N of 3 to radio frequency interference (RFI), and we masked both the on-burst and off-burst spectra. The ACFs of both the on-burst and the off-burst spectra were then computed using

$$\mathrm{ACF}(\Delta\nu) = \frac{\sum_i (S(\nu_i) - \overline{S})(S(\nu_i + \Delta\nu) - \overline{S})}{N_{\Delta\nu}(\overline{S} - \overline{S}_{\mathrm{noise}})^2}, \quad (1)$$

following ref. 28. We only sum over indices i that give non-masked values for the S/N measurements $S(\nu_i)$ and $S(\nu_i + \Delta\nu)$ at a given i. $N_{\Delta\nu}$ is the total number of unmasked overlapping frequency channels that are used to compute the ACF for a given frequency lag $\Delta\nu$. The ACF calculated using equation (1) is normalized such that the amplitude of a characteristic frequency scale present in the ACF is the square of the modulation index of that frequency scale, where the modulation index is defined as the standard deviation of the observed burst spectrum divided by its mean[25].

In Fig. 1, we show the on-burst ACF for FRB 20221022A for the entire observing bandwidth, with the zero lag noise spike masked and with three clear frequency scales visible by eye. There is a 27.3-MHz frequency scale arising from CHIME's instrumental design[20], which we can see by eye in the dynamic spectrum (Extended Data Fig. 1). We fit the ACF out to a lag of 20 MHz with a triple Lorentzian function

$$\frac{m_1^2}{1 + (\Delta\nu/\gamma_1)^2} + \frac{m_2^2}{1 + (\Delta\nu/\gamma_2)^2} + \frac{m_3^2}{1 + (\Delta\nu/\gamma_3)^2}, \quad (2)$$

for frequency lag $\Delta\nu$, the Lorentzian half-width at half-maximum γ_i and modulation index m_i. We note that a Lorentzian is the expected functional form of the ACF, with the decorrelation bandwidth defined as the half-width at half-maximum of the Lorentzian, to mathematically obtain a temporal exponential decay from scatter broadening[25]. We note that a quasi-periodic spectral structure was observed in spectra of FRB 20121102A and was suggested to arise from diffractive lensing[38]. As we know that the instrumental ripple is not scintillation, we do not necessarily expect that it should adopt the functional form of a Lorentzian. The exact functional form we fit to the instrumental ripple scale is unimportant as long as we capture the amplitude of the modulation. This is because the frequency scale is orders of magnitude different from the other two scales evident in the ACF, and so only the amplitude of the modulation at the frequency lags relevant for the smaller frequency scales (that is, around the peak) is important to return reliable modulation indices (the difference between, for example, a Lorentzian or Gaussian at such small frequency lags is indistinguishable). We consider correlated uncertainties in the ACF, following ref. 39 and the implementation in scintools[40], which are propagated into the fitting procedure. We compute the reduced-χ^2 statistic between lags ±0.25 MHz, relevant for the 2 smaller frequency scales, which probably could be scintillation, and find that 3 Lorentzians fit well to the data with a reduced χ^2 of 0.95. The potential decorrelation bandwidths, defined as the half-width at half-maximum of the Lorentzian, are measured to be 3.18 ± 0.04 kHz and 60.3 ± 0.7 kHz, with modulation indices $m \approx 1.3$ and $m \approx 0.89$, respectively (Fig. 1; that is, in the ACF of the full CHIME bandwidth). We note that these frequency scales are smaller than the decorrelation bandwidths we measure in the frequency-resolved ACFs (see following paragraph and Fig. 2) owing to the burst having a larger S/N in the lower half of the band (where the decorrelation bandwidth is smaller): that is, these values are S/N weighted.

Residual upchannelization artefacts as well as RFI can introduce misleading frequency structure in the spectrum ACF. To test that the frequency scales that we measure in the on-burst ACF across the entire CHIME band are consistent with scintillation, we divide the 400-MHz total bandwidth into 8 subbands, containing an equal fraction of the burst energy, and compute the ACF per subband to explore the frequency dependence of the putative scintillation. As described above, we normalize the ACF using the mean of the spectrum. For the subbanded ACFs, we normalize using the mean of the spectrum within each subband, which coarsely corrects for a frequency-dependent burst fluence. We measure both frequency scales in all eight subbands using a double Lorentzian fit per subband (Fig. 2). The uncertainties on the ACF fit parameters are a quadrature sum of the fit uncertainties with the finite-scintle error, following the implementation in scintools[40]. As shown in Fig. 2, we perform a least-squares fit of a function of the form $A\nu^\alpha$ to the half-width at half-maxima measured from the two Lorentzians fit to the ACF, for constant A and index α. To confirm the frequency scales observed are scintillation, we expect $\alpha \approx 4$, whereas an instrumental artefact or RFI should not evolve with frequency in the same manner. It is noted that we omit the high-frequency data point, as it cannot be distinguished from the 390-kHz upchannelization artefact (Fig. 2). For the smaller frequency scale, we measure $\alpha = 3.7 \pm 0.6$, and for the larger scale we measure $\alpha = 3.2 \pm 0.3$. The 6-kHz frequency scale shows a frequency dependence consistent with the ν^4 scaling for refractive scattering, whereas the frequency dependence of the 128-kHz scale is shallower (but within the range observed for pulsar scintillation[41]). We therefore attribute both scales to scintillation from two scattering screens along the line of sight from FRB 20221022A to the observer. We report decorrelation bandwidths of 6 ± 1 kHz and 128 ± 6 kHz at 600 MHz, which we measure from the $A\nu^\alpha$ fits, and with uncertainties determined using the standard deviation of the fit residuals. It is worth noting that decorrelation-bandwidth measurements of individual bursts from a single source at the same observing epoch can have large scatter, for example, ref. 42. This is a result of varying S/N per burst and low number of scintles $O(10)$, which is encompassed in the very large uncertainties for these bursts. In this work, FRB 20221022A is at the high end of the S/N ratios reported in ref. 42, with $O(1000)$ scintles, resulting in smaller uncertainties on the decorrelation bandwidth.

As noted earlier, the frequency scales that we measure in the full-band ACF are markedly smaller than those we measure in the subbanded analysis. This is owing to the fact that the burst is brighter in the lower part of the band where the decorrelation bandwidth is smaller, as well

as the fact that there are more scintles in the bottom part of the band compared with the top. It is possible that these effects are still skewing our decorrelation-bandwidth measurements within each subband, affecting both the decorrelation bandwidth and frequency evolution. To explore what effect, if any, this has on our measurements, we simulate an FRB spectrum with measured decorrelation bandwidth 104 kHz at 600 MHz, and frequency index $\alpha = 3.95$. We then simulate 100 spectra with the same input parameters, apply the same RFI mask and divide the band into the same 8 subbands as we apply to the real data. We then perform the same analysis: ACF per subband, then fit $A\nu^{\alpha}$ to the half-width at half-maxima of the ACFs. We find that the simulations are consistent within the uncertainties of our measurements (Extended Data Fig. 3). We therefore conclude that the subbanding and RFI masking is not significantly skewing our measurements.

The NE2001 decorrelation-bandwidth prediction[23,24] at 1 GHz in this line of sight is about 400 kHz. We scale our decorrelation bandwidths using the measured frequency scaling index α, giving $\Delta\nu_{\mathrm{DC,1GHz}} \approx 40$ kHz and $\Delta\nu_{\mathrm{DC,1GHz}} \approx 656$ kHz. The 6-kHz and 128-kHz decorrelation bandwidths are a factor of about 10 lower and about 1.6 higher than the NE2001 prediction, respectively.

In addition to measuring the modulation index in the entire band ACF, we also measure the modulation indices across the burst profile in time and across the observing band. In Extended Data Fig. 1, we plot the modulation index measured across the burst profile in time bins of width 164 μs. These modulation indices are measured by computing the ACF of the spectra (averaged over 164 μs of time) with frequency resolution 24 kHz, and taking the square root of the peak subtracting a constant offset (introduced by the instrumental ripple). We choose this frequency resolution to ensure that the 6-kHz frequency scale is unresolved and reducing its influence on the modulation index measurements. It is noted that in Extended Data Fig. 1, we plot only the modulation index measurements where the S/N within the 164 μs time interval was >8. The modulation index broadly appears to be constant over the burst duration, with a mean of 0.76 ± 0.06.

Two-screen constraints

We consider a two-screen system as shown in Extended Data Fig. 4, with the observer, $\oplus$, an astrophysical point source (here, FRB 20221022A), $\star$, and two screens: s_1 (closest to the observer) and s_2 (closest to the source). We are following the formalism derived in refs. 17,43 for an extragalactic source, but deriving it generally to allow for a Galactic source (see, for example, ref. 44). The temporal broadening timescale of an FRB at distance $d_{\oplus\star}$, scattered by the screen s_2 at distance $d_{\oplus\mathrm{s}_2}$ from the observer, and distance $d_{\mathrm{s}_2\star}$ from the FRB source, is

$$\tau_{\mathrm{s}_2} = \frac{\theta_{\mathrm{s}_2}^2}{c}\frac{d_{\oplus\star}d_{\oplus\mathrm{s}_2}}{d_{\mathrm{s}_2\star}}, \tag{3}$$

where θ_{s_2} is the angular-broadened size of the FRB scattered by screen s_2 and c is the speed of light[43]. The coherence length of the radio waves incident on screen s_1 is

$$l_{\mathrm{c}} \simeq \frac{\lambda}{2\pi\theta_{\mathrm{s}_2}} = \frac{\lambda}{2\pi}\sqrt{\frac{d_{\oplus\star}d_{\oplus\mathrm{s}_2}}{\tau_{\mathrm{s}_2}\, c\, d_{\mathrm{s}_2\star}}}, \tag{4}$$

for observing wavelength λ. Scattering from screen s_2 can weaken scintillation from s_1 if the coherence length is reduced below the size of the Galactic scattering projected onto s_1:

$$l_{\mathrm{cone}} \simeq d_{\oplus\mathrm{s}_1}\theta_{\mathrm{s}_1} \simeq \sqrt{\tau_{\mathrm{s}_1}\, c\frac{d_{\mathrm{s}_1\star}d_{\oplus\mathrm{s}_1}}{d_{\oplus\star}}}. \tag{5}$$

With a measurement of scattering or scintillation (at least one scintillation scale is required) from both screens in the two-screen system, this sets the condition that $l_{\mathrm{c}} \gtrsim l_{\mathrm{cone}}$, yielding:

$$\tau_{\mathrm{s}_1}\tau_{\mathrm{s}_2} \lesssim \frac{1}{(2\pi\nu)^2}\frac{d_{\oplus\star}^2 d_{\oplus\mathrm{s}_2}}{d_{\mathrm{s}_1\star}d_{\mathrm{s}_2\star}d_{\oplus\mathrm{s}_1}}. \tag{6}$$

Using the relation between the scatter-broadening timescale, τ, and decorrelation bandwidth from scintillation $\Delta\nu_{\mathrm{DC}}$: $\tau = \frac{C}{2\pi\Delta\nu_{\mathrm{DC}}}$ with $C \approx 1$–2, we derive the general two-screen equation:

$$\Delta\nu_{\mathrm{s}_1}\Delta\nu_{\mathrm{s}_2} \gtrsim C_{\mathrm{s}_1}C_{\mathrm{s}_2}\nu^2\frac{d_{\mathrm{s}_1\star}d_{\mathrm{s}_2\star}d_{\oplus\mathrm{s}_1}}{d_{\oplus\star}^2 d_{\oplus\mathrm{s}_2}}. \tag{7}$$

The high posterior probability (>99%)[10] of the host-galaxy association confirms that FRB 20221022A is extragalactic. We must consider whether the two screens we observe are both Galactic, or if one of the screens is extragalactic. With our two measured scintillation scales in hand, we consider both of these cases below.

One extragalactic screen and one Galactic screen

First, let us assume that the screen s_2 is extragalactic, and s_1 is a screen within the Milky Way. In this situation, we have the approximations

$$d_{\oplus\star} \simeq d_{\oplus\mathrm{s}_2} \simeq d_{\mathrm{s}_1\star} \tag{8}$$

and so we can simplify equation (7) to

$$\Delta\nu_{\mathrm{s}_1}\Delta\nu_{\mathrm{s}_2} \gtrsim C_{\mathrm{s}_1}C_{\mathrm{s}_2}\nu^2\frac{d_{\mathrm{s}_2\star}d_{\oplus\mathrm{s}_1}}{d_{\oplus\star}^2}. \tag{9}$$

It is noted that typically there is a $(1+z)$ factor here[45], which we do not include as the redshift of FRB 20221022A is sufficiently small ($z = 0.0149$)[10] that it does not affect the results.

Given our scintillation measurements for FRB 20221022A: 6 kHz and 128 kHz, assuming $C_{\mathrm{s}_1} = C_{\mathrm{s}_2} = 1$, which is the most conservative value in this case, and taking the distance to the identified host galaxy in ref. 10, $d_{\oplus\star} = 65.189$ Mpc, we get the constraint:

$$d_{\oplus\mathrm{s}_1}d_{\mathrm{s}_2\star} \lesssim 9.1\ \mathrm{kpc}^2 \tag{10}$$

Using NE2001[23,24], we can estimate $d_{\oplus\mathrm{s}_1}$ from the distance where the wavenumber spectral coefficient C_n^2 peaks (which can be thought of as a quantity resembling the amount of turbulence): $d_{\oplus\mathrm{s}_1} \approx 0.64$ kpc. This gives us the constraint $d_{\mathrm{s}_2\star} \lesssim 14.1$ kpc. It is worth noting that this prediction of $d_{\oplus\mathrm{s}_1}$ is highly uncertain, and we consider its impact on $d_{\mathrm{s}_2\star}$ and ultimately our emission-region size constraints later.

Furthermore, the decorrelation-bandwidth measurement can be used to place a limit on the individual screen distances[46]. Starting with equation (47) in ref. 46 and assuming Kolmogorov turbulence[47], we derive

$$\Delta\nu_{\mathrm{s}_2} \approx \pi\nu\left(\frac{l_{\mathrm{diff}}}{R_{\mathrm{F}}}\right)^2, \tag{11}$$

where l_{diff} is the diffraction length, or the length through the screen over which the phase changes by 1 radian, and $R_{\mathrm{F}} = cd_{\mathrm{s}_2\star}/\nu$ is the Fresnel radius. Equation (19) in ref. 48 gives the relationship between l_{diff} and the phase change across the screen ϕ

$$l_{\mathrm{diff}} \approx \phi^{-6/5}\, l_{\mathrm{max}}\left(\frac{L}{l_{\mathrm{max}}}\right)^{3/5}, \tag{12}$$

for the thickness of the screen L and the maximum eddy size in the scattering medium l_{max}. ϕ is directly proportional to the dispersion measure of the screen (column depth within the thickness of the screen), $\mathrm{DM}_{\mathrm{s}_2}$, with the relationship equation (17) in ref. 48

$$\phi = \frac{2.6\times10^{7}\ \mathrm{DM}_{s_2}}{\nu_{\mathrm{GHz}}}. \quad (13)$$

Combining all of these relationships into equation (11), we arrive at (see also equation (57) in ref. 46):

$$\mathrm{DM}_{s_2} \approx 3\times10^{4}\ \mathrm{pc\ cm^{-3}}\ \Delta\nu_{s_2}^{-5/12}\ \nu_{\mathrm{GHz}}^{11/6}\left(\frac{d_{s_2\star}}{1\ \mathrm{pc}}\right)^{5/12}\left(\frac{l_{\max}}{L}\right)^{1/3}\left(\frac{L}{d}\right)^{5/6}. \quad (14)$$

Substituting in our measured decorrelation bandwidth $\Delta\nu_{s_2}$ = 128 kHz, observing frequency $\nu_{\mathrm{GHz}} = 0.6$, and taking the ratio of maximum eddy size over screen size to be $l_{\max}/L \approx 10^{-4}$ (consistent with what is seen from Milky Way turbulence):

$$\mathrm{DM}_{s_2} \approx 4\ \mathrm{pc\ cm^{-3}}\left(\frac{d_{s_2\star}}{1\ \mathrm{pc}}\right)^{5/12}\left(\frac{L}{d_{s_2\star}}\right)^{5/6}.$$

The contribution of the total dispersion measure attributed to the host galaxy was estimated in ref. 10 as $\mathrm{DM_{host}} \lesssim 14^{+23}_{-14}$ pc cm^{-3}. We therefore estimate the following:

$$(0\text{–}37)\ \mathrm{pc\ cm^{-3}} \gtrsim \mathrm{DM}_{s_2} \approx 4\ \mathrm{pc\ cm^{-3}}\left(\frac{d_{s_2\star}}{1\ \mathrm{pc}}\right)^{5/12}\left(\frac{L}{d_{s_2\star}}\right)^{5/6}$$

and so

$$\left(\frac{d_{s_2\star}}{1\ \mathrm{pc}}\right) \lesssim 210\ \mathrm{pc}\left(\frac{L}{d_{s_2\star}}\right)^{-2}.$$

If we assume that $\frac{L}{d_{s_2\star}} \approx 1$, we have a tight constraint on $d_{s_2\star} < 210$ pc. However, $\frac{L}{d_{s_2\star}} \approx 1$ is not always a fair assumption, with values inferred $\ll 1$ for some pulsars[49–51]. This therefore, unfortunately, does not tightly constrain the distance $d_{s_2\star}$.

Two Galactic screens

Now we assume that the source is extragalactic, at a distance[10] of $d_{\oplus\star}$ = 65.189 Mpc, but both screens s_1 and s_2 are within the Milky Way. Given this situation, we can make the approximations:

$$d_{s_1\star} \simeq d_{s_2\star} \simeq d_{\oplus\star}.$$

Under this approximation, the assumption that $C_{s_1} = C_{s_2} = 1$ and using our decorrelation-bandwidth measurements, equation (7) gives the constraint:

$$\frac{d_{\oplus s_1}}{d_{\oplus s_2}} \lesssim \frac{\Delta\nu_{s_1}\Delta\nu_{s_2}}{C_{s_1}C_{s_2}\nu^2} \approx 2\times10^{-9}. \quad (15)$$

Even if we force $d_{\oplus s_2}$ to be the isophotal diameter of the Milky Way, about 27 kpc (ref. 52), this restricts $d_{\oplus s_1}$ to be $\lesssim$0.0001 pc: it is highly unlikely that there is a screen within such close proximity to us. It is worth noting that FRB 20221022A is about 64° off the ecliptic, and therefore one of the scintillation scales coming from the solar wind can be easily ruled out. If we change $d_{\oplus s_2}$ to be smaller, the condition in equation (15) forces $d_{\oplus s_1}$ to be even smaller, supporting that this outcome is highly unlikely.

We note that if we consider the case where both screens are extragalactic, the problem is symmetric and the same constraint applies. Suppose the farther screen is 50 kpc from the source, out in the host galaxy's halo, then the nearby screen would need to be <0.0001 pc. Although pulsars are known to scintillate from bow shocks very close to the source[53], this configuration is much more fine-tuned and therefore more unlikely than the case where one of the screens is Galactic. Throughout this section, we have implicitly assumed that the screens are two-dimensional and isotropic. The ACF in Fig. 1 is well fit with a double Lorentzian function. We therefore find no deviations from the expectations of the isotropic screen assumption. Deviations from these expectations, however, can be subtle, and so we explore below the possibility of one-dimensional anisotropic screens and the implications for our conclusions.

One-dimensional anisotropic screens

Throughout this paper, the implicit assumption we make is that the scintillation screens are isotropic and two-dimensional. This assumption means that the angular broadening of the source owing to the screen closest to the observer is equivalent to the size of the source as seen by the farther screen. However, if the screens are sheet-like[19] (that is, the normal vector of the 'sheet' is perpendicular to the line of sight, rather than parallel in the case of the thin-screen model), the angular broadening is direction dependent, introducing a dependence on the angle between the one-dimensional screens. The condition $l_c \gtrsim l_{\mathrm{cone}}$ from the subsection above, becomes $l_c \gtrsim l_{\mathrm{cone}}\cos(\theta)$, where θ is the angle between the two sheet-like screens projected onto the line-of-sight plane.

For the two Galactic screens described above, equation (15) becomes

$$\frac{d_{\oplus s_1}}{d_{\oplus s_2}}\cos^2(\theta) \lesssim \frac{\Delta\nu_{s_1}\Delta\nu_{s_2}}{C_{s_1}C_{s_2}\nu^2} \approx 2\times10^{-9}. \quad (16)$$

For reasonable $d_{\oplus s_1}$ and $d_{\oplus s_2}$, this inequality can be satisfied by invoking a $\cos(\theta) \ll 1$, or equivalently making the one-dimensional screens almost perfectly perpendicular. This is very tightly constraining the geometry of the scattering media, which is fine-tuned in reality and therefore unrealistic. In addition, as discussed in the following section, for the larger scintillation scale, with modulation index <1, we find the decorrelation bandwidth and modulation index frequency dependence to agree more with the emission size being resolved than the screens resolving each other. These frequency dependencies are not affected by the $\cos(\theta)$ term and therefore add further doubt to the scenario of an extragalactic source with two almost perpendicular one-dimensional Galactic screens.

In ref. 19, it is shown that one can observe a suppression of the modulation index for the larger scintillation scale if the finer scintillation scale is unresolved by the telescope frequency resolution. However, this situation does not apply to this work as we have resolved both scintillation scales in our analysis.

Suppressed intensity modulation

The case studies presented above support the extragalactic nature of the second screen, s_2. The two-screen constraints in equation (10) place the second screen likely within the host galaxy. We observe no clear frequency or time evolution of the modulation index of the 128-kHz scintillation scale (Fig. 2 and Extended Data Fig. 1). The modulation index for FRB 20221022A was observed to decrease over the burst profile (which is dominated by an exponential scattering tail) owing to the two screens partially resolving each other[44]. In the case presented here, we are not resolving the scattering timescale, and so it is not surprising that we do not observe an evolution of the modulation index with time. We explore the possibility that the modulation index $m_{128\mathrm{kHz}} < 1$ observed is either owing to the screens resolving each other or owing to the emission-region size being resolved. We note that in the case of weak scintillation[25], one can expect $m_{\mathrm{weak}} \approx 0.1\text{–}0.3$, which is lower than our measurement of $m_{128\mathrm{kHz}} \approx 0.78$. When the source or screen is resolved, different scintillation patterns are effectively being averaged. This has the effect of smearing the scintillation pattern in frequency and suppressing the amplitude of the intensity modulation. For this

reason, in both of these cases we expect different modulation index and decorrelation-bandwidth frequency dependencies, which we derive below.

First we derive the relationship for the case where the observed emission-region size is being partially resolved.

The physical size of the extragalactic screen, s_2, is

$$L_{s_2} = \theta_{s_2} d_{s_2\star}, \tag{17}$$

where θ_{s_2} is the angular size of screen s_2 from the perspective of the FRB source, and

$$\theta_{s_2} = \sqrt{\frac{2c\tau_{s_2}}{d_{s_2\star}}} = \sqrt{\frac{c}{\pi \Delta\nu_{s_2} d_{s_2\star}}}, \tag{18}$$

where we relate the scattering timescale and decorrelation bandwidth through the relation $\tau_{s_2} \approx 1/(2\pi\Delta\nu_{s_2})$. Substituting equation (18) into equation (17) yields:

$$L_{s_2} = \sqrt{\frac{c d_{s_2\star}}{\pi \Delta\nu_{s_2}}}. \tag{19}$$

The physical resolution of the screen is then

$$\chi_{s_2} = \frac{1}{\sqrt{2}\pi}\frac{\lambda}{L_{s_2}} d_{s_2\star} = \frac{1}{\nu}\sqrt{\frac{c d_{s_2\star}\Delta\nu_{s_2}}{2\pi}}, \tag{20}$$

where the $\frac{1}{\sqrt{2}\pi}$ is a model-dependent factor[12].

Substituting equation (20) into[13]

$$m_{s_2} = \frac{1}{\sqrt{1 + 4\left(\frac{R_{\star\mathrm{obs}}}{\chi_{s_2}}\right)^2}}, \tag{21}$$

where $R_{\star\mathrm{obs}}$ is the observed emission-region size, we derive the relationship between the lateral emission-region size and the distance between the source and extragalactic screen:

$$R_{\star\mathrm{obs}} = \sqrt{\frac{c\, d_{s_2\star}\, \Delta\nu_{s_2}(\nu)}{8\pi\nu^2}\left(\frac{1}{m_{s_2}^2} - 1\right)}. \tag{22}$$

Following a similar line of reasoning, we derive an equivalent relationship for the case where the two screens are partially resolving each other:

$$m_{s_2} = \frac{1}{\sqrt{1 + \left(\frac{\nu}{d_{s_1 s_2}}\right)^2 \frac{8\, d_{s_2\star}\, d_{\oplus s_1}}{\Delta\nu_{s_1}(\nu)\Delta\nu_{s_2}(\nu)}}} \tag{23}$$

In Fig. 2, we plot the least-squares fit of the modulation indices as a function of frequency with their expected relationships: equation (22) for the partially resolved emission-region size, and equation (23) for the two screens partially resolving each other. It is evident that in the case of the two screens resolving each other, we expect a stronger frequency dependence than what is observed, suggesting that the data are more in agreement with the case of the emission region being partially resolved (although neither fit describes the data with our measured reduced $\chi^2 > 1$: quantitatively we measure reduced $\chi^2_\nu \approx 139$ for the resolving screens, and reduced $\chi^2_\nu \approx 97$ for the emission region being resolved). We note that these functional forms can become more complex by invoking a complicated morphological structure of the scattering material, which is one reason why the fits may be poor. Another reason could be that the modulation index of the 128-kHz scintillation scale is suppressed by an aspect of the analysis performed, for example, during the upchannelization artefact removal process. We additionally consider the case where the modulation index is 1; however, as we show later, this is less conservative for the emission-region size constraints than using the $m_{s_2} \approx 0.78$ measurement.

For both scenarios, we now derive the decorrelation-bandwidth frequency dependencies. From equation (46) in ref. 13

$$\nu_{\mathrm{scint}} = \frac{\sqrt{1 + 4\sigma_1^2}}{2\pi\tau_s}, \tag{24}$$

where $\sigma_1 = R_{\star\mathrm{obs}}/\chi_{s_2}$ for the case where the emission region is being resolved (see equation (21)), and $\sigma_1 = L_{s_2}/\chi_{s_1}$ for the case where the screen is being resolved. First let us consider a partially resolved emission region. In this case, $\chi_{s_2} \propto \nu$ (see equation (20)), which in turn means that $\sigma_1 \propto \nu^{-1}$. From equation (24), this then gives the following frequency dependence:

$$\nu_{\mathrm{scint}} \propto \sqrt{A\nu^8 + B\nu^6} \tag{25}$$

for constants A and B. In the case where the screen is being resolved, $L_{s_2} \propto \nu^{-2}$ (see equation (19)), $\chi_{s_1} \propto \nu$ (from equation (20)), which then results in $\sigma_1 \propto \nu^{-3}$. From equation (24), this then gives the following frequency dependence:

$$\nu_{\mathrm{scint}} \propto \sqrt{C\nu^8 + D\nu^2}. \tag{26}$$

for constants C and D. For completely unresolved emission, the first term in both equations (25) and (26) dominates, and we arrive at the ν^4 frequency scaling for the decorrelation bandwidth. However, if the scintillation is (partially) resolved, the second term dominates. For the emission region being resolved, the frequency dependence becomes $\nu_{\mathrm{scint}} \propto \nu^3$ and for the screens resolving each other we arrive at $\nu_{\mathrm{scint}} \propto \nu$. Our measured frequency scaling of $\alpha = 3.2 \pm 0.3$ for the 128-kHz scintillation scale (Fig. 2) supports that the emission-region size is being partially resolved. $\alpha = 4$, that is, the case where the emission region is unresolved, is $>3\sigma$ inconsistent.

Emission size constraints

As outlined in ref. 9, a measurement of scintillation from a screen in the FRB host galaxy can be used to constrain the size of the FRB emission region, which in turn could be used to distinguish between FRB emission models. The 128-kHz modulation index frequency evolution and decorrelation-bandwidth frequency relation supporting the emission-region size being partially resolved suggests that the 128-kHz scintillation scale is a result of the extragalactic screen, s_2. The high reduced χ^2 of the modulation index versus frequency fit, as well as the inconsistency with the NE2001 prediction, as mentioned earlier, means that we cannot rule out the scenario where neither the emission region nor the screen is being partially resolved. We, therefore, consider all cases here: (1) 128-kHz scintillation scale from the extragalactic screen, that is partially resolving the emission region, $m_{128\mathrm{kHz}} = 0.78$; (2) 128-kHz scintillation scale from the extragalactic screen, with an unresolved emission region, $m_{128\mathrm{kHz}} \approx 1$; and (3) 6-kHz scintillation scale from the extragalactic screen, with an unresolved emission region, $m_{6\mathrm{kHz}} \approx 1$.

In Fig. 3, we plot the lateral emission size as a function of the extragalactic screen distance for case 1: which is the case our data agrees with most, while also being the most conservative constraint on the emission-region size. There is a clear degeneracy between the lateral emission-region size and the FRB to extragalactic screen distance, which naturally arises as the $m_{s_2} \approx 0.78$ measurement fixes the projected size of the emission region on the screen. As shown earlier, we have a constraint on the screen distance, $d_{s_2\star} < 14.1$ kpc (equation (9); assuming $d_{\oplus s_1} = 0.64$ kpc, from NE2001[23]). With this limit, we can see from Fig. 3 that the lateral emission size upper limit is lower than the estimated size for the non-magnetospheric models[5–8]. However, this

hinges on the Galactic screen distance we have assumed from the NE2001 estimate, which can be highly uncertain. To have consistency with non-magnetospheric models, we require an extragalactic screen distance of ≥144 kpc (Fig. 3), and a Galactic screen distance of ≲63 pc (Extended Data Fig. 5). This screen configuration is extremely unlikely for three main reasons: (1) using equations (4) and (5) from ref. 9, we estimate the electron density at a distance of 144 kpc given our scintillation measurements to be $O(10^{-3})$ cm^{-3}, which is at least an order of magnitude larger than current best estimates of the Milky Way at the same distance[29]; (2) it is unlikely for the Galactic screen to be within 63 pc (for example, ref. 54) and there are no known H II regions or nearby stars that could explain the nearby screen; and (3) we would have to invoke an FRB source living outside of the galaxy disk to explain why we do not measure scattering or scintillation from the disk itself, which has higher densities. We, therefore, place an upper limit on the FRB to screen distance of 11 kpc, which is the apparent diameter of the host galaxy[30]. It is worth noting that this apparent diameter is derived from optical observations, whereas the electron distribution will extend farther; however, the inclination of the galaxy with respect to the line of sight, as well as the low inferred host dispersion measure[10] make it highly unrealistic that FRB 20221022A propagated through the full extent of the Galactic disk, making this upper limit very conservative. With this upper limit on the screen distance, we place the conservative constraint on the lateral emission-region size of $R_{\star\mathrm{obs}} \lesssim 3 \times 10^4$ km.

It is worth noting that there are two foreground stars[55] at distances of about 0.5 kpc and about 0.8 kpc (broadly consistent with the $d_{\oplus s_1}$ = 0.64 kpc estimate from NE2001) coincident with the FRB position and host galaxy, identified in ref. 10. These stars could create a scintillation screen from their stellar winds, as has been observed for hot stars[56] extending out to about 2 pc: the projected area on the sky would encompass the entire host galaxy and FRB localization region. The two foreground stars in the FRB 20221022A field, however, are lower temperature than those observed in ref. 56 and so would have a lower mass loss rate and the surroundings would have a lower density. A stellar wind screen could explain the inferred larger density than the NE2001 prediction for the case where the 6-kHz scintillation scale is the Galactic scale, which is about 10 times lower—that is, an approximately 10 times higher scattering timescale—compared with NE2001. However, without very long baseline interferometry (VLBI) to constrain the Galactic screen distance and geometry, we cannot confirm that the stellar wind is causing the Galactic scintillation here.

Finally, let us consider cases (2) and (3) above. In both of these cases, we assume $m_{s_2} \approx 1$, which tells us that the emission region is a point source as viewed from the extragalactic screen. This, therefore, constrains only a minimum distance between the FRB and extragalactic screen for a given source size (Extended Data Fig. 6). The allowable lateral emission-region size and screen distance combinations are shown in Extended Data Fig. 6 in green and blue for case 2 and case 3, respectively. To have an emission-region size consistent with the shock model[7], we require $d_{s_2\star} > 12$ Mpc and $d_{s_2\star} > 250$ Mpc for case 2 and case 3, respectively. As the FRB is at a distance of 65 Mpc, the non-magnetospheric model cannot work for case 3. There is no obvious nearby galaxy with a halo that could conceivably intersect the FRB line of sight, and so a scattering screen >12 Mpc from the FRB is highly unlikely. Moreover, this requires a Galactic screen distance ≲1 pc given our two-screen constraints (equation (9)), which is unreasonably close, especially as FRB 20221022A is about 64° off the ecliptic, and therefore we can rule out the Galactic scintillation scale arising from the solar wind.

Given our observed emission-region size constraints, our observations disfavour the non-magnetospheric FRB models (for example, refs. 5–8). Our results are more consistent with the magnetospheric class of FRB emission models[9] or emission originating just beyond the light cylinder of a neutron star (for example, refs. 15,31). This supports the findings of ref. 10, where we measure a polarization angle S-shaped swing in FRB 20221022A, which has been attributed to a beam sweeping across the observers line of sight, therefore tying the emission site to the rotation of an object.

Assuming an emission-region size comparable to those observed in pulsars (100–1,000 km; refs. 15,57), motivated by the pulsar-like polarization angle swing[10], we infer an extragalactic screen distance from the source of 0.1–12 pc (Fig. 3), consistent with the size of the Crab Nebula[58].

European VLBI Network imaging

If we assume an emission size typical for pulsar emission, 100–1,000 km (refs. 15,57), we infer an extragalactic screen distance of 0.1–12 pc (Fig. 3), comparable in scale to the size of the Crab Nebula[58]. Three repeating FRBs in the literature have been observed associated with compact persistent radio sources (PRSs)[59–63]. The nature of these radio counterparts is debated in the literature, with one of the competing theories being magnetized nebulae surrounding the FRB progenitor[64]. Motivated by the possibility that the scintillation scale is coming from a surrounding nebula, we observed the field of FRB 20221022A with the European VLBI Network (EVN) to search for any compact radio emission (project ID RN002). These observations were conducted during an e-VLBI session, where the data were correlated in real-time using SFXC[65] at the Joint Institute for VLBI ERIC (JIVE). We observed with the EVN from 9 April 2024 22:01:55 UT to 10 April 2024 04:22:30 UT, with the following participating stations: Jodrell Bank Mark2, Effelsberg, Medicina, Noto, Onsala (On-85), Tianma (T6), Toruń and Irbene. The central observing frequency of our observations is 1.6 GHz, with a bandwidth of 128 MHz. The interferometric data were correlated with time and frequency integration of 2 s and 0.5 MHz, respectively. We correlated the target data at the position right ascension (J2000) = 03 h 14 min 17.4 s, declination (J2000) = 86° 52′ 01″, which is consistent with the centre of FRB 20221022A's associated host galaxy[10]. In addition to the target scans, we observed J0217+7349 as the flux and bandpass calibrator, J0213+8717 as the phase calibrator (at a spatial separation of 0.89° from the pointing centre) and J0052+8627 as the check source. Traditional phase-referencing observations were conducted with a cycle time of 6.5 min: 5 min on target, 1.5 min on the phase calibrator. In total, we observed the field of FRB 20221022A for 4 hours. We note that we did not get target data with On-85 owing to the high elevation of the source.

Raw voltage data were recorded from each participating telescope with circular polarization feeds and 2-bit sampling in VDIF[66] format. The correlated visibilities were calibrated and imaged using standard procedures in the Astronomical Image Processing System[67] and DIFMAP[68]. First, using the results of the automatic EVN pipeline (https://evlbi.org/handling-evn-data), we performed amplitude calibration using the gain curves and individual station system temperature measurements, applied the bandpass calibration, and performed some basic flagging. We then performed some additional manual flagging of the fringe finder, before removing the instrumental delay. The final step of the calibration was to correct the phases for the entire observation, as a function of time and frequency, by performing a fringe fit using the calibrator sources. Throughout, we use Effelsberg, the most sensitive telescope in our array, as the reference antenna.

After calibration, we imaged the check source to confirm that we detected it as a point source, as expected, and at the correct sky position. We then performed a grid search ±102 arcseconds around the target phase centre. This grid search comprised making dirty maps of 2 × 2 arcseconds spanning the entire 102 × 102 arcsecond grid, and reporting the peak of each dirty map. We made dirty maps using both natural and uniform weighting, resulting in beam sizes of 3.6 × 6.9 mas and 2.2 × 4.6 mas, respectively. The resulting root mean square (rms) noise levels are 42 μJy per beam and 63 μJy per beam for the natural and uniform weighted images, respectively. Given our shortest baseline (Irbene-to-Toruń; approximately 452 km), we are resolving out radio emission with size larger than approximately 82 mas.

Owing to time and frequency smearing, we can expect to lose sensitivity as we move farther from the phase centre. Across the extent of the host galaxy, we expect to lose at most 10% of the sensitivity, whereas at the edge of the 1σ FRB baseband localization[10] we lose around 30%. We did not detect any persistent compact radio emission in our search, down to a luminosity limit of $L_{1.6\mathrm{GHz}} < 2 \times 10^{27}$ erg s^{-1} Hz^{-1} (7σ). There is a possible 6.6σ candidate at the edge of the FRB 3σ localization region that is not detected in the The Very Large Array Sky Survey (VLASS)[69]. Confirming the astrophysical nature of this candidate is deferred to future work, but given its 3σ offset from the FRB position, and large offset from the host galaxy, it seems unlikely to be related to FRB 20221022A. We confirm that the National Radio Astronomy Observatory VLA Sky Survey (NVSS) source reported in ref. 10, NVSS J031417+865200, co-located with the centre of the FRB host galaxy is resolved out on our long baselines. This supports their conclusion that it is from star formation in the host galaxy. With our sensitivity, we could have detected all three known PRSs with a significance ranging from approximately 15σ to >1,000σ. Our upper limit is in agreement with the proposed PRS luminosity–rotation measure relation[70], given the relatively low measured rotation measure for FRB 20221022A (rotation measure −40 rad m^{-2})[10].

Effelsberg single-dish FRB search

Although FRB 20221022A is an as-yet non-repeating FRB, we recorded high-time-resolution search data with Effelsberg in parallel to search for possible repeat bursts. These search data was recorded at Effelsberg during the target scans in psrfits format using the Effelsberg Direct Digitization backend, with a time and frequency resolution 49.2 µs and 0.12 MHz, respectively. The bandwidth of these data is from 1.5 GHz to 1.75 GHz, that is, an observing band of 250 MHz. The total intensity psrfits data from the Effelsberg Direct Digitization backend were converted to filterbank format using digifil[71], conserving the time and frequency resolution of the psrfits data. This was done to be compatible with Heimdall (https://sourceforge.net/projects/heimdall-astro/), which we use for the single-pulse search. Before performing the burst search, we masked frequency channels that were found to contain RFI. Single-pulse candidates above an S/N threshold of 7 identified by Heimdall were then classified using FETCH (models A and H, with a probability threshold of 0.5)[72]. The FETCH candidates as well as the Heimdall candidates with dispersion measures in the range of 115–118 pc cm^{-3} were inspected by eye. We found no promising FRB candidates above an S/N of 7. Using the radiometer equation[73], taking the typical Effelsberg system temperature and gain values as 20 K and 1.54 K Jy^{-1}, respectively, and assuming a burst width of 1 ms, we arise at the fluence upper limit of 0.1 Jy ms for this observation. Owing to the sporadic activity behaviour of repeating FRBs (for example, ref. 74), our non-detection cannot confirm that FRB 20221022A will never repeat in the future.

Rise and decay times

As discussed in ref. 10, the burst shows no clear evidence for temporal broadening owing to multi-path propagation, with an upper limit of $\tau_s < 550$ µs at 400 MHz. The decorrelation-bandwidth measurements presented in this work are consistent with this upper limit: the smallest decorrelation bandwidth, 6 kHz, corresponds to the larger temporal broadening scale through the relation $\tau_s \approx C/(2\pi\Delta\nu_{DC})$, which gives a scatter-broadening timescale of approximately 112 µs at 400 MHz. This confirms that the burst morphology is dominated by the intrinsic burst decay time, as opposed to the exponential decay from scatter broadening, as indicated by the scattering upper limits presented in ref. 10. Both the rise and decay times can be important quantities for probing the burst emission physics[46]. For example, it is difficult to explain extremely short temporal variations in non-magnetospheric FRB models[33,46].

Data availability

The beamformed baseband CHIME FRB data presented in this work are available on Zenodo at https://doi.org/10.5281/zenodo.13954067 (ref. 75). The European VLBI Network data are available on the JIVE archive (project ID RN002).

Code availability

We have made the spectral analysis code available at the following GitHub repository: https://github.com/KenzieNimmo/FRB20221022A_scintillation.

38. Levkov, D. G., Panin, A. G. & Tkachev, I. I. Propagation effects in the FRB 20121102A spectra. *Astrophys. J.* **925**, 109 (2022).
39. Brockwell, P. J. & Davis, R. A. *Time Series: Theory and Methods* (Springer, 1991).
40. Reardon, D. J. et al. Precision orbital dynamics from interstellar scintillation arcs for PSR J0437–4715. *Astrophys. J.* **904**, 104 (2020).
41. Geyer, M. et al. Scattering analysis of LOFAR pulsar observations. *Mon. Not. R. Astron. Soc.* **470**, 2659–2679 (2017).
42. Nimmo, K. et al. Milliarcsecond localization of the repeating FRB 20201124A. *Astrophys. J. Lett.* **927**, L3 (2022).
43. Ocker, S. K. et al. The large dispersion and scattering of FRB 20190520B are dominated by the host galaxy. *Astrophys. J.* **931**, 87 (2022).
44. Sammons, M. W. et al. Two-screen scattering in CRAFT FRBs. *Mon. Not. R. Astron. Soc.* **525**, 5653–5668 (2023).
45. Macquart, J.-P. & Koay, J. Y. Temporal smearing of transient radio sources by the intergalactic medium. *Astrophys. J.* **776**, 125 (2013).
46. Beniamini, P. & Kumar, P. What does FRB light-curve variability tell us about the emission mechanism? *Mon. Not. R. Astron. Soc.* **498**, 651–664 (2020).
47. Bhat, N. D. R., Cordes, J. M., Camilo, F., Nice, D. J. & Lorimer, D. R. Multifrequency observations of radio pulse broadening and constraints on interstellar electron density microstructure. *Astrophys. J.* **605**, 759–783 (2004).
48. Beniamini, P., Kumar, P. & Narayan, R. Faraday depolarization and induced circular polarization by multipath propagation with application to FRBs. *Mon. Not. R. Astron. Soc.* **510**, 4654–4668 (2022).
49. Walker, M. A., Koopmans, L. V. E., Stinebring, D. R. & van Straten, W. Interstellar holography. *Mon. Not. R. Astron. Soc.* **388**, 1214–1222 (2008).
50. Brisken, W. F. et al. 100 µas resolution VLBI imaging of anisotropic interstellar scattering toward pulsar B0834+06. *Astrophys. J.* **708**, 232–243 (2010).
51. Serafin Nadeau, T. et al. A cacophony of echoes from daily monitoring of the Crab Pulsar at Jodrell Bank. *Astrophys. J.* **962**, 57 (2024).
52. Goodwin, S. P., Gribbin, J. & Hendry, M. A. The relative size of the Milky Way. *The Observatory* **118**, 201–208 (1998).
53. Ocker, S. K. et al. Pulsar scintillation through thick and thin: bow shocks, bubbles, and the broader interstellar medium. *Mon. Not. R. Astron. Soc.* **527**, 7568–7587 (2024).
54. Stock, A. M. & van Kerkwijk, M. H. Associations between scattering screens and interstellar medium filaments. Preprint at https://arxiv.org/abs/2407.16876 (2024).
55. Gaia Collaboration et al. Gaia data release 3. Summary of the content and survey properties. *Astron. Astrophys.* **674**, A1 (2023).
56. Walker, M. A. et al. Extreme radio-wave scattering associated with hot stars. *Astrophys. J.* **843**, 15 (2017).
57. Gwinn, C. R. et al. Size of the Vela Pulsar's emission region at 18 cm wavelength. *Astrophys. J.* **758**, 7 (2012).
58. Hester, J. J. The Crab Nebula : an astrophysical chimera. *Ann. Rev. Astron. Astrophys.* **46**, 127–155 (2008).
59. Chatterjee, S. et al. A direct localization of a fast radio burst and its host. *Nature* **541**, 58–61 (2017).
60. Marcote, B. et al. The repeating fast radio burst FRB 121102 as seen on milliarcsecond angular scales. *Astrophys. J. Lett.* **834**, L8 (2017).
61. Niu, C. H. et al. A repeating fast radio burst associated with a persistent radio source. *Nature* **606**, 873–877 (2022).
62. Bhandari, S. et al. Constraints on the persistent radio source associated with FRB 20190520B using the European VLBI Network. *Astrophys. J. Lett.* **958**, L19 (2023).
63. Bruni, G. et al. A nebular origin for the persistent radio emission of fast radio bursts. *Nature* **632**, 1014–1016 (2024).
64. Margalit, B. & Metzger, B. D. A concordance picture of FRB 121102 as a flaring magnetar embedded in a magnetized ion-electron wind nebula. *Astrophys. J. Lett.* **868**, L4 (2018).
65. Keimpema, A. et al. The SFXC software correlator for very long baseline interferometry: algorithms and implementation. *Exp. Astron.* **39**, 259–279 (2015).
66. Whitney, A., Kettenis, M., Phillips, C. & Sekido, M. VLBI Data Interchange Format (VDIF). In *Sixth International VLBI Service for Geodesy and Astronomy. Proc. 2010 General Meeting* (eds Navarro, R. et al.) 192–196 (Springer, 2010).
67. Greisen, E. W. in *Information Handling in Astronomy—Historical Vistas* Astrophysics and Space Science Library Vol. 285 (ed. Heck, A.) 109–125 (2003).
68. Shepherd, M. C., Pearson, T. J. & Taylor, G. B. DIFMAP: an interactive program for synthesis imaging. *Bull. Am. Astron. Soc.* **26**, 987–989 (1994).
69. Lacy, M. et al. The Karl G. Jansky Very Large Array Sky Survey (VLASS). Science case and survey design. *Publ. Astron. Soc. Pac.* **132**, 035001 (2020).
70. Yang, Y.-P., Li, Q.-C. & Zhang, B. Are persistent emission luminosity and rotation measure of fast radio bursts related? *Astrophys. J.* **895**, 7 (2020).
71. van Straten, W. & Bailes, M. DSPSR: digital signal processing software for pulsar astronomy. *Publ. Astron. Soc. Aust.* **28**, 1–14 (2011).

72. Agarwal, D., Aggarwal, K., Burke-Spolaor, S., Lorimer, D. R. & Garver-Daniels, N. FETCH: a deep-learning based classifier for fast transient classification. *Mon. Not. R. Astron. Soc.* **497**, 1661–1674 (2020).
73. Cordes, J. M. & McLaughlin, M. A. Searches for fast radio transients. *Astrophys. J.* **596**, 1142–1154 (2003).
74. Lanman, A. E. et al. A sudden period of high activity from repeating fast radio burst 20201124A. *Astrophys. J.* **927**, 59 (2022).
75. Nimmo, K., Magnetospheric origin of a fast radio burst constrained using scintillation Dataset. *Zenodo* https://doi.org/10.5281/zenodo.13954067 (2024).

Acknowledgements We thank B. Marcote for help with the EVN observations; R. Karuppusamy for help with the pulsar backend recording at Effelsberg; D. Jow for discussions about anisotropic screens; J. Cordes and S. Ocker for answering questions about NE2001; and J. Hessels for discussions. K.N. is an MIT Kavli Fellow. Z.P. was a Dunlap Fellow and is supported by an NWO Veni fellowship (VI.Veni.222.295). P.B. is supported by a grant (number 2020747) from the United States-Israel Binational Science Foundation (BSF), Jerusalem, Israel by a grant (number 1649/23) from the Israel Science Foundation and by a grant (number 80NSSC 24K0770) from the NASA astrophysics theory programme. P.K. is supported in part by an NSF grant AST-2009619 and a NASA grant 80NSSC24K0770. M.W.S. acknowledges support from the Trottier Space Institute Fellowship programme. A.P.C. is a Vanier Canada Graduate Scholar. The Dunlap Institute is funded through an endowment established by the David Dunlap family and the University of Toronto. B.M.G. acknowledges the support of the Natural Sciences and Engineering Research Council of Canada (NSERC) through grant RGPIN-2022-03163, and of the Canada Research Chairs programme. V.M.K. holds the Lorne Trottier Chair in Astrophysics and Cosmology, a Distinguished James McGill Professorship, and receives support from an NSERC Discovery grant (RGPIN 228738-13), from an R. Howard Webster Foundation Fellowship from CIFAR, and from the FRQNT CRAQ. C.L. is supported by NASA through the NASA Hubble Fellowship grant HST-HF2-51536.001-A awarded by the Space Telescope Science Institute, which is operated by the Association of Universities for Research in Astronomy, Inc., under NASA contract NAS5-26555. K.W.M. holds the Adam J. Burgasser Chair in Astrophysics and is supported by NSF grants (2008031 and 2018490). A.P. is funded by the NSERC Canada Graduate Scholarships – Doctoral programme. A.B.P. is a Banting Fellow, a McGill Space Institute (MSI) Fellow, and a Fonds de Recherche du Quebec – Nature et Technologies (FRQNT) postdoctoral fellow. K.S. is supported by the NSF Graduate Research Fellowship Program. FRB research at UBC is supported by an NSERC Discovery Grant and by the Canadian Institute for Advanced Research. The baseband recording system on CHIME/FRB is funded in part by a CFI John R. Evans Leaders Fund grant to IHS. We thank the directors and staff at the various participating EVN stations for allowing us to use their facilities and running the observations. The European VLBI Network is a joint facility of independent European, African, Asian and North American radio astronomy institutes. Scientific results from data presented in this publication are derived from the following EVN project code: RN002.

Author contributions K.N. led the data analysis, interpretation and writing of the paper. Z.P. guided the analysis, and contributed to the interpretation and writing. P.B. and P.K. suggested the search for scintillation in CHIME FRBs, and contributed to the emission physics interpretation. A.E.L., D.Z.L., R.M. and M.W.S. provided substantial guidance regarding the analysis strategy, the mathematical framework and the interpretation of the results. S.A., M.B., S.C., A.P.C., E.F., B.M.G., R.C.J., Z.K., V.M.K., M.L., C.L., K.W.M., R.M., D.M., A.P., A.B.P., M.R.-R., K.R.S., K. Shin, K. Smith and I.H.S. contributed to the discovery of the FRB source and acquisition of data through the building or maintenance of the CHIME telescope and commented on the paper.

Competing interests The authors declare no competing interests.

Additional information
Supplementary information The online version contains supplementary material available at https://doi.org/10.1038/s41586-024-08297-w.
Correspondence and requests for materials should be addressed to Kenzie Nimmo.
Peer review information *Nature* thanks Casey Law and Di Li for their contribution to the peer review of this work. Peer reviewer reports are available.

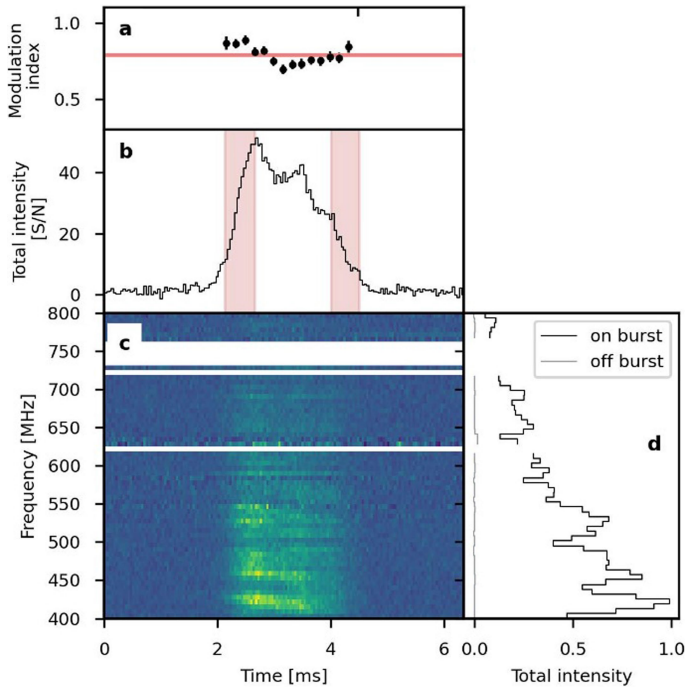

Extended Data Fig. 1 | FRB 20221022A burst dynamic spectrum (panel c), profile (panel b), spectrum (panel d) and modulation index (panel a). The burst is dedispersed to a dispersion measure[10] of 116.837 pc cm^{-3} and is plotted with time and frequency resolution 40.96 μs and 6.2 MHz, respectively. The rise and decay time are highlighted using the shaded red regions in **b**. Both the on-burst time-averaged spectrum and off-burst spectrum are shown in **d**. For each 163.84 μs time bin, we compute the ACF (equation (1)) across frequency (ACF is computed for spectra with a frequency resolution of 24 kHz), and measure the modulation index as the height of the Lorentzian fit to the ACF around zero lag. We only plot modulation indices for 163.84 μs time bins that have a S/N > 8 (**a**). The mean of the measured time resolved modulation indices for the 128 kHz scintillation scale is shown with the red line in **a**, and is measured to be $\overline{m} = 0.76 \pm 0.06$, consistent with the frequency-resolved modulation index measured for this scintillation scale.

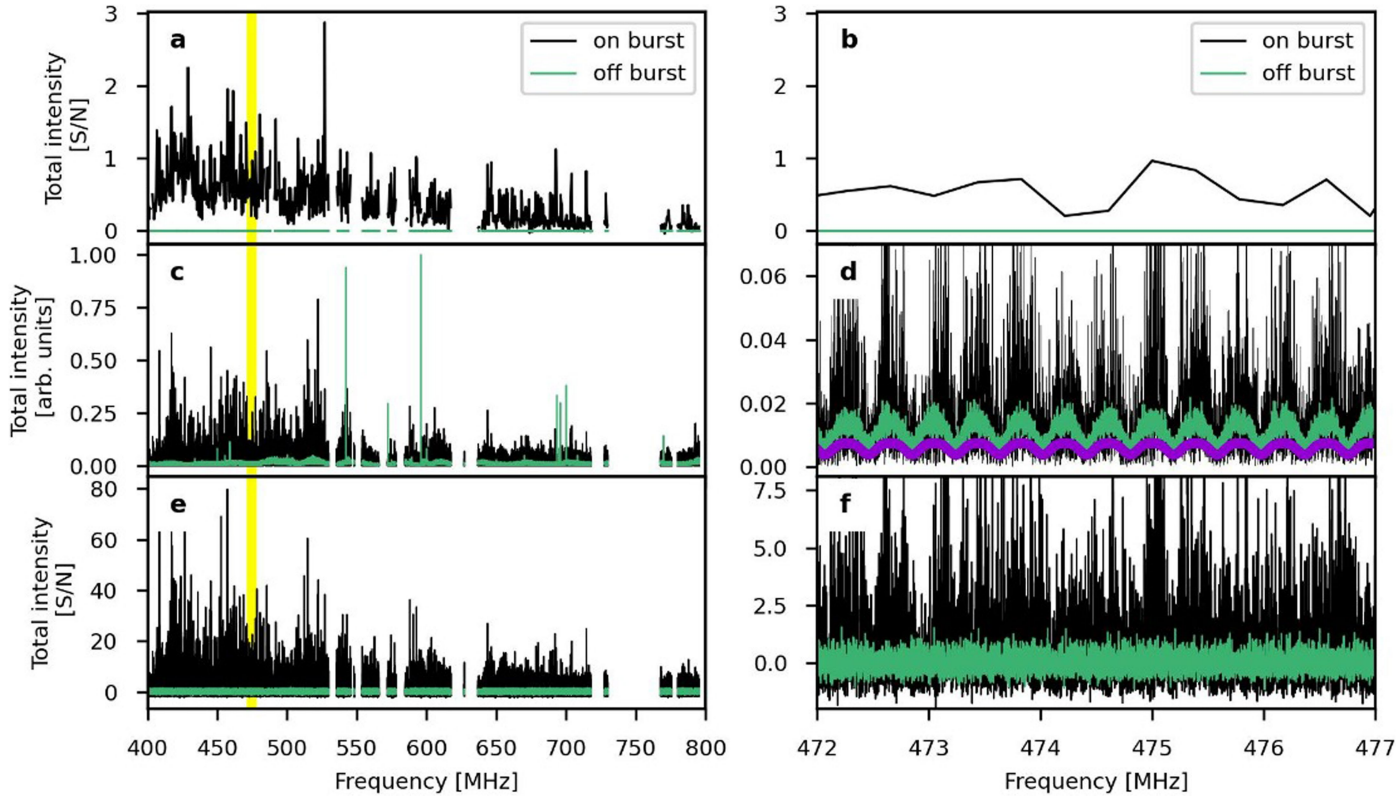

Extended Data Fig. 2 | On-burst and off-burst spectra across the CHIME observing band from 400–800 MHz (panels a,c,e). A zoom-in around 472–477 MHz (the yellow bar in **a**,**c**,**e**) is plotted in **b**,**d**,**f**. Panels **a** and **b** are the spectra of the baseband data with frequency resolution 0.39 MHz (1024 channels across the entire observing band). The upchannelized spectra (frequency resolution: 0.76 kHz) are shown in **c** and **d** *before* correcting for the scalloping introduced by the FFT. The model we use to correct the scalloping is shown in purple in **d**. Panels **e** and **f** show the spectra after correcting for the upchannelization scalloping, and applying additional RFI masking.

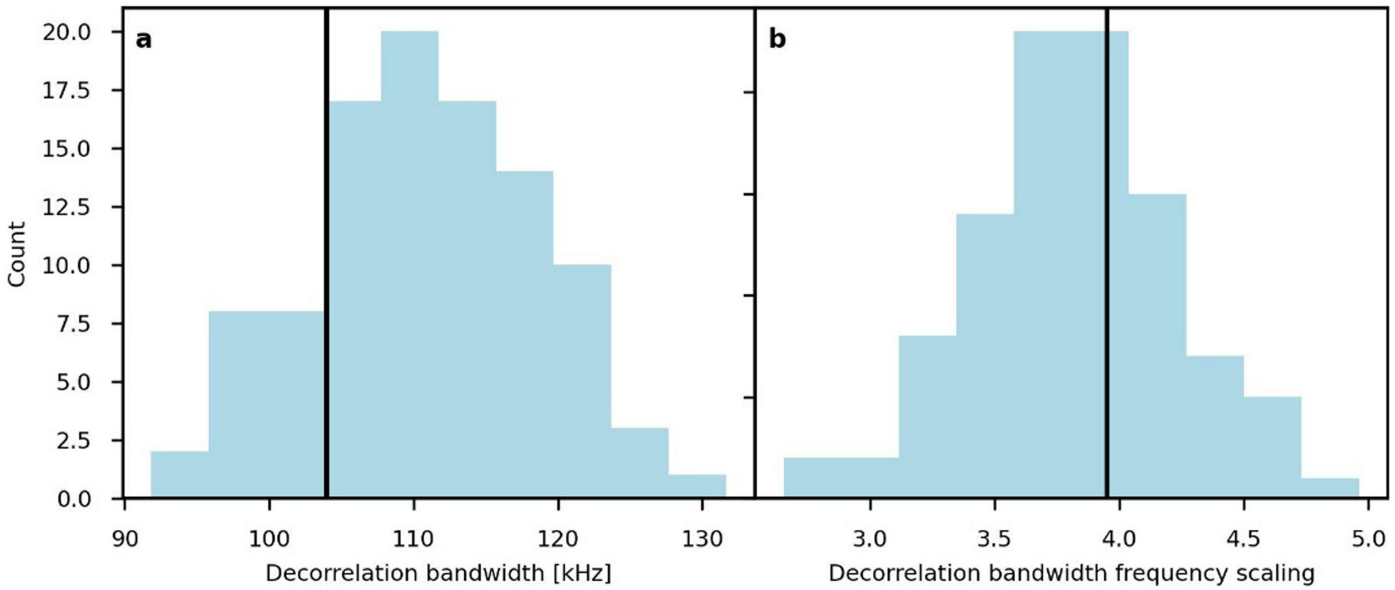

Extended Data Fig. 3 | Decorrelation bandwidth and corresponding frequency dependence measured from 100 simulated FRB spectra using the same input parameters, and utilising the same RFI mask and subband edges as used in the analysis of FRB 20221022A. a, Measured decorrelation bandwidths in the simulations. The black line is the decorrelation bandwidth measurement of a simulated spectrum using the same input parameters but without RFI masking and using equal frequency width subbands. Similarly, **b** shows the measured decorrelation bandwidth frequency indices, comparing again with the measurement from a simulated spectrum without RFI masking and using equal width subbands (black line).

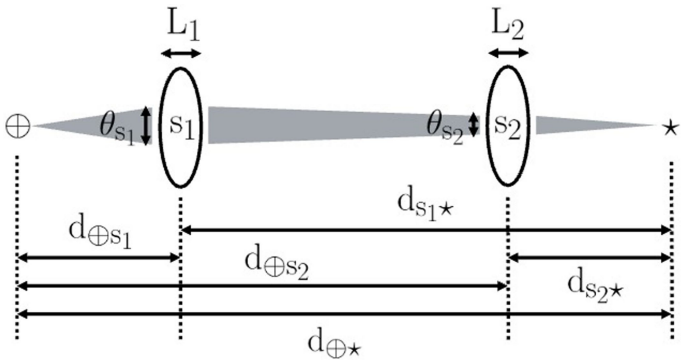

Extended Data Fig. 4 | Diagram of a two-screen lensing setup. The relevant distances, d, length scales, L, and angular broadening angles, θ are shown relating the source ($\star$), screen nearest the source (s_2), screen nearest the observer (s_1) and observer.

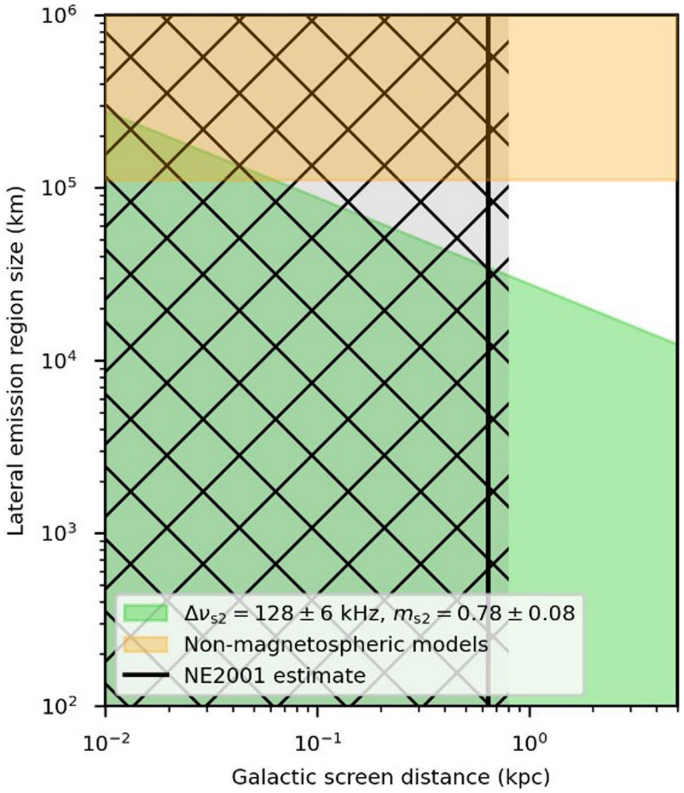

Extended Data Fig. 5 | The lateral emission region size as it depends on the Galactic screen distance, $d_{\oplus s1}$, through the relationship shown on Fig. 3 and the two-screen constraint in equation (9). The green shaded region shows the allowable lateral emission region sizes and Galactic screen distance combinations for our measured scintillation parameters at 600 MHz: $\Delta\nu_{s2}$ = 128 kHz and m_{s2} = 0.78. The black vertical line indicates the NE2001 prediction[23]: $d_{\oplus s1}$ = 0.64 kpc. The orange shaded region shows the emission region sizes estimated for non-magnetospheric models[5–8]. The grey hatched region shows the parameter space we ruled out based on the apparent diameter of the host galaxy (see Fig. 3).

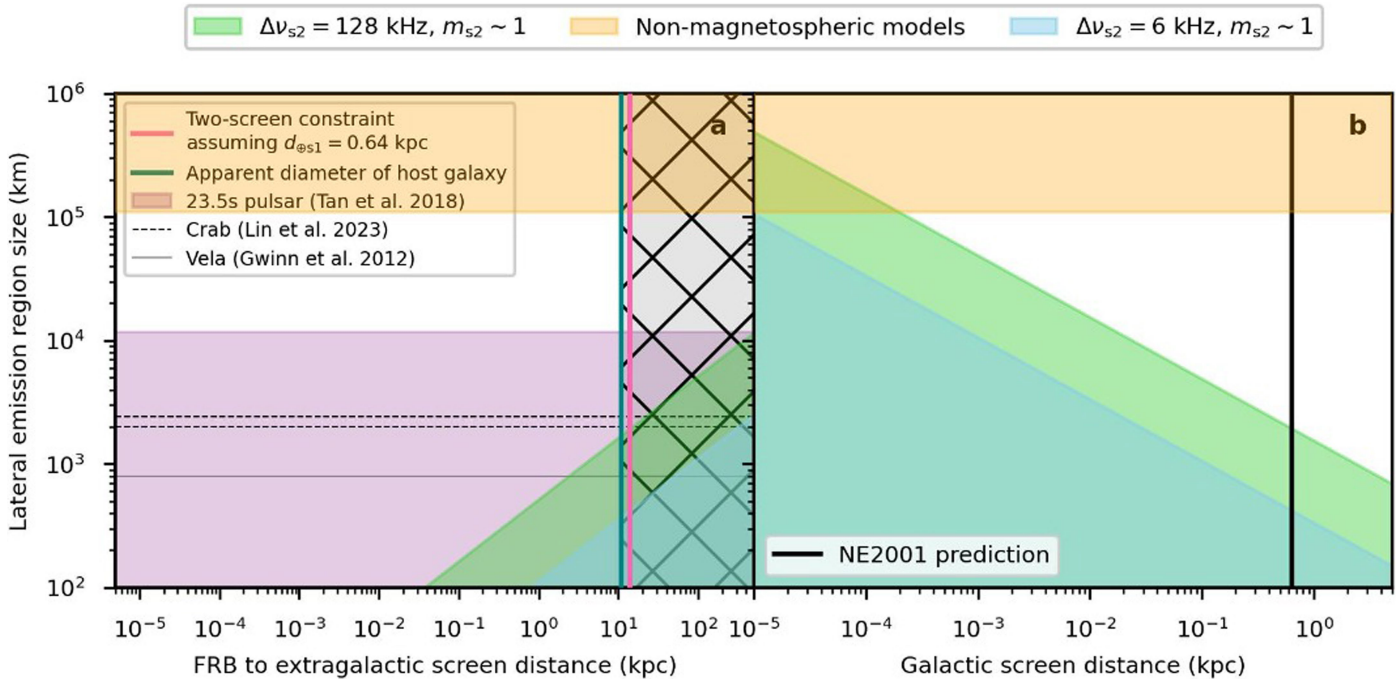

Extended Data Fig. 6 | Lateral emission region size constraints for the other cases we consider. Case (2) in the text refers to the extragalactic screen having a decorrelation bandwidth of 128 kHz at 600 MHz and a modulation index of 1 (green shaded region); and case (3) for the extragalactic screen having a decorrelation bandwidth of 6 kHz at 600 MHz and a modulation index of 1 (blue shaded region). Panel **a** is the same as Fig. 3 (case (1)) for different scintillation measurements (case (2) and case (3)), and panel **b** is the same as Extended Data Fig. 5 for the additional cases considered.